Improved Localization Precision and Angular Resolution of a Cylindrical, Time-Encoded Imaging System From Adaptive Detector Movements

Niral P. Shah, *Member, IEEE*, Peter Marleau, *Member, IEEE*, Jeffrey A. Fessler, *Fellow, IEEE*, David L. Chichester, *Senior Member, IEEE*, and David K. Wehe, *Senior Member, IEEE*

***Abstract*— To the first order, the localization precision and angular resolution of a cylindrical, time-encoded imaging (c-TEI) system is governed by the geometry of the system. Improving either measure requires increasing the mask radius or decreasing the detector diameter, both of which are undesirable. We propose an alternative option of repositioning the detector within the mask to increase the detector-to-mask distance in the direction of a source, thereby improving the localization precision and angular resolution in that direction. Since the detector-to-mask distance only increases for a small portion of the field of view (FOV), we propose implementing adaptive imaging where one leverages data collected during the measurement to optimize the system configuration. This article utilizes both simulations and experiments to set upper bounds on the potential gain from adaptive detector movements for one and two sources in the FOV. When only one source is present, adaptive detector movements can improve the localization precision and angular resolution by 20% for a source at 90 cm and by 32% for a far-field source. When two sources are present, adaptive detector movements can improve localization precision and angular resolution by up to 50% for sources that are ∼10° apart (90 cm from the system). We experimentally verify these results through maximum likelihood estimation of the source position(s) and image reconstruction of point sources that are close together. As a demonstration of an adaptive imaging algorithm, we image a complex arrangement of special nuclear material at the Zero Power Physics Reactor facility at Idaho National Laboratory.**

***Index Terms*— Adaptive imaging, angular resolution, cylindrical time-encoded imaging (c-TEI), fast neutron imaging, gamma-ray imaging, source localization.**

Manuscript received October 10, 2020; revised December 20, 2020; accepted January 12, 2021. Date of publication February 18, 2021; date of current version April 16, 2021. This work was supported in part by the Nuclear Nonproliferation International Safeguards Fellowship Program sponsored by the Department of Energy, National Nuclear Security Administration's Office of International Nuclear Safeguards under Grant NA-241, in part by the Consortium for Verification Technology through the Department of Energy National Nuclear Security Administration under Award DE-NA0002534, in part by the Consortium for Monitoring, Technology, and Verification through the Department of Energy National Nuclear Security Administration, USA, under Award DE-NA0003920, and in part by the Sandia National Laboratories, a multimission laboratory managed and operated by National Technology and Engineering Solutions of Sandia, LLC, a wholly owned subsidiary of Honeywell International Inc., for the U.S. Department of Energy's National Nuclear Security Administration under Contract DE-NA0003525. Approved for unlimited release SAND2021-1208J.

Niral P. Shah was with the Nuclear Engineering and Radiological Sciences Department, University of Michigan, Ann Arbor, MI 48109 USA (e-mail: nirpshah@umich.edu).

Peter Marleau is with the Sandia National Laboratories, Livermore, CA 94550 USA (e-mail: pmarlea@sandia.gov).

Jeffrey A. Fessler is with the Department of Electrical Engineering and Computer Science, University of Michigan, Ann Arbor, MI 48109 USA (e-mail: fessler@umich.edu).

David L. Chichester is with the Idaho National Laboratory, Idaho Falls, ID 83415 USA (e-mail: david.chichester@inl.gov).

David K. Wehe is with the Nuclear Engineering and Radiological Sciences Department, University of Michigan, Ann Arbor, MI 48109 USA (e-mail: dkw@umich.edu).

Color versions of one or more figures in this article are available at https://doi.org/10.1109/TNS.2021.3060071.

Digital Object Identifier 10.1109/TNS.2021.3060071

I. Introduction

UNCERTAINTY when estimating the location of a source, that is, localization precision, and angular resolution are important performance measures when designing an imaging system for many nuclear nonproliferation and international safeguards applications. For example, high localization precision is valuable when localizing lost or hidden nuclear material [1], [2]. In the context of warhead counting, high angular resolution is necessary to separate and count multiple warheads on a missile and may aid in verifying the extent of the warheads [3]–[5].

Due to their relative simplicity and low cost, there is growing interest in using cylindrical, time-encoded imaging (c-TEI) systems for these applications [6]–[10]. The focus of this work is on improving the localization precision and angular resolution of c-TEI systems to make them better suited for these types of applications.

A. Cylindrical, Time-Encoded Imaging

A conventional c-TEI system consists of a nonposition-sensitive detector placed at the center of a rotating, cylindrical, coded mask. As the mask rotates, the intervening material between the detector and the source changes and temporally encodes the source distribution into the count rate observed by the detector. One can use this time-dependent data alongside the orientation and design of the mask to reconstruct the source scene.

Practically speaking, improving localization precision and angular resolution in a conventional c-TEI system requires either increasing the mask radius or reducing the detector size. Design parameters such as the width of a unit mask element or the mask pattern also play an important role, but since the width of a unit mask element is usually chosen

0018-9499 © 2021 IEEE. Personal use is permitted, but republication/redistribution requires IEEE permission.
See https://www.ieee.org/publications/rights/index.html for more information.

Authorized licensed use limited to: University of Michigan Library. Downloaded on April 18,2021 at 16:44:55 UTC from IEEE Xplore. Restrictions apply.

based on the detector size [10] and the pattern based on its periodic auto-correlation function [11], they are usually not manipulated to improve localization precision and angular resolution.

Localization precision depends on the difference in responses between the true source location and its nearby neighbors [12]. When the detector is centered, this dependence translates to the sharpness of open-to-closed (or closed-to-open) mask element transitions. For the same mask pattern, increasing the mask radius or reducing the detector size makes those transitions sharper [8] and thus improves localization precision. With respect to angular resolution, to the first order, two sources are deemed resolvable if they are separated by the angular width of a unit mask element. Thus, the angular resolution changes with mask radius and detector size. Practically, changing either parameter is undesirable since increasing the mask radius can make the system unwieldy in terms of physical size and reducing the detector size decreases efficiency.

As an alternative to these options, we propose repositioning the detector within the surrounding mask to achieve better localization precision and angular resolution for a limited field-of-view (FOV). As shown in Fig. 1, when the detector is repositioned from the center of the mask (D_c) to an off-center position (D_o), the detector-to-mask distance increases along the axis pointing from the center of the detector to the center of the mask. We refer to this axis as the imaging axis. This increase in detector-to-mask distance results in sharper mask element transitions and decreases the angular separation at which two sources are separated by the width of a unit mask element ($\theta_o < \theta_c$), thus both localization precision and angular resolution improve.

Since the detector-to-mask distance does not increase in all directions, the localization precision and angular resolution for sources that are not close to the imaging axis may be worse than in the conventional, detector-centered case. Thus, the optimal detector position depends on the source location which may not be known prior to the experiment. To address this problem, we propose implementing adaptive imaging.

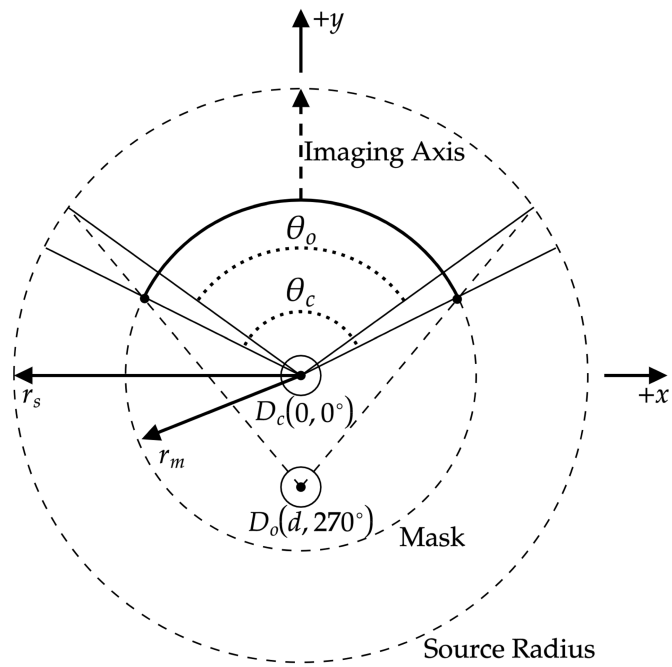

Fig. 1. Top-down view of a c-TEI system with a centered detector (D_c) and an off-center detector (D_o). An exaggerated closed unit mask element is shown at $\theta = 90°$ as a solid arc at a mask radius of r_m. By repositioning the detector from D_c to D_o, the detector-to-mask distance increases along the imaging axis. This increase in the detector-to-mask distance results in sharper mask element transitions and decreases the angular separation at which two sources are separated by the width of a unit mask element ($\theta_o < \theta_c$), thus both localization precision and angular resolution improve for sources near the imaging axis.

B. Adaptive Imaging

As shown in Fig. 2, in adaptive imaging, an imaging system or data acquisition protocol is modified during the measurement based on collected data. For example, given that the user has no prior information, a c-TEI system first collects a scout scan with the detector at the center and uses that information to estimate relevant parameters such as the source location and intensity. Next, a planning algorithm predicts the performance of the system for the possible detector positions and repositions the detector to maximize performance for some or all of the sources hypothesized to be present. The system then collects another revolution of data and the cycle repeats until the user intervenes or a termination condition, such as elapsed time, ends the cycle. With adaptive imaging, the system can reposition the detector to any position inside the mask and improve its performance based on the hypothesized source scene.

Adaptive imaging is an active area of research in astronomy [13], [14], medical imaging [15]–[20], and emergency response [21], [22]. Within terrestrial nuclear imaging, Willcox *et al.* [23] investigated the value of adaptively orienting a rotating modulation collimator to position a source in the highest performance region of the FOV. Their results show higher quality reconstructions when imaging a single point source. Additionally, Fitzgerald *et al.* [24] built a liquid spatial coded aperture (SCA) system where the mask pattern is controlled by automated plungers filled with liquid metal such that the mask pattern can be changed at any time during measurement. They found that reconstructions made using sequences of random masks have greater a signal-to-noise ratio (SNR) than those made using traditional mask patterns. We are unaware of any previous work on adaptive imaging with c-TEI systems.

C. Defining the Problem

Since there are numerous adaptive imaging schemes that could be implemented, this article focuses on setting an upper bound on the potential improvement to localization precision and angular resolution from adaptive detector movements. To establish this upper bound, we conduct a clairvoyant analysis. By clairvoyant, we mean that all of the model parameters, such as the number of sources, are known beforehand so that there is no added uncertainty

Authorized licensed use limited to: University of Michigan Library. Downloaded on April 18,2021 at 16:44:55 UTC from IEEE Xplore. Restrictions apply.

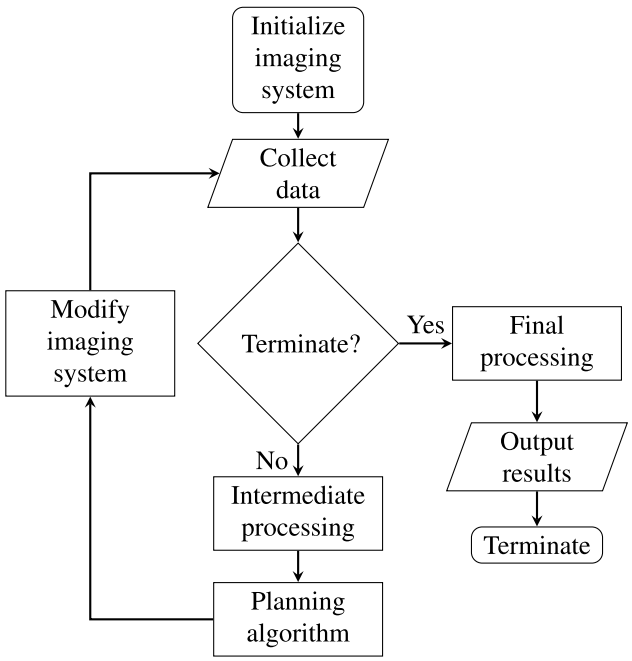

Fig. 2. Adaptive imaging flowchart.

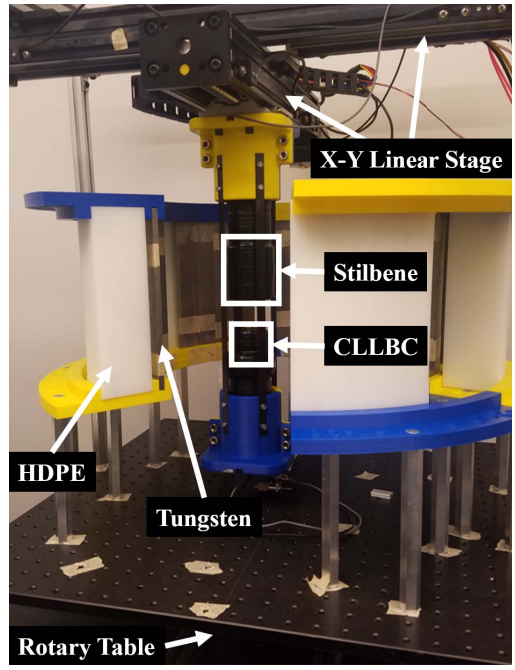

Fig. 3. Photograph of the MATADOR imaging system.

from detection and estimation. We consider the following scenarios:

1) one point source and
2) two point sources at various separations and differing emission intensities.

For each scenario, we find the detector position that maximizes the improvement in localization precision and angular resolution relative to the centered case. We also consider the additional benefit from combining data from two off-center detector positions instead of just one off-center detector position. Most of the analysis is done using simulations, but we use experimental data to verify the methodology and demonstrate the improved localization precision and angular resolution.

Section II describes the MATADOR imaging system that we built to test and verify these concepts. Section III provides some necessary nomenclature for the clairvoyant analysis and introduces the objective functions used to find the optimal detector positions. Section IV presents the benefit of collecting data at one off-center detector position for one point source and Section V presents the same for two point sources. Section VI discusses the value of combining data from two off-center detector positions for both one and two point sources. Finally, Section VII presents a demonstration of these techniques on a complex arrangement of special nuclear material at the zero power physics reactor (ZPPR) facility at Idaho National Laboratory (INL).

II. MATADOR Imaging System

The MATADOR imaging system is a 1-D, dual-particle, adaptive c-TEI system. The design for MATADOR is very similar to the c-TEI system described in [8], thus this section only provides a brief overview of the system shown in Fig. 3.

MATADOR utilizes a dual-layer mask and two nonposition-sensitive detectors to image both gamma rays and fast neutrons. To modulate gamma rays, the inner layer of the mask is made of 0.635 cm of tungsten, and to modulate fast neutrons, the outer layer is made of 6 cm of high-density polyethylene. Both mask layers are arranged in a uniformly redundant array pattern with 35 elements, thus the angular width of an element is $\sim$10.3° [11]. The outer radius of the mask is 25.7 cm, and MATADOR can collect a full revolution of data in 90 s.

To detect both particles, MATADOR utilizes two detectors: a 1" $Cs_2LiLa(Br, Cl)_6$ (CLLBC) detector [25] to detect gamma rays and a 2" stilbene detector [26] to detect fast neutrons. One could also use the gamma rays detected by the stilbene detector to reconstruct gamma-ray images but the lack of photopeaks would increase the background. Thus, we prefer to use the CLLBC data for gamma-ray reconstructions. Except for the content in Section VII, all of the analysis and results in this article are for fast neutrons detected with the stilbene detector. The demonstration in Section VII uses gamma-ray data from the CLLBC detector.

The two detectors hang from an x–y linear stage such that the detectors can move to any position inside the mask. Notice in Fig. 3 that the detectors are fixed along the z-axis such that they cannot move independently. Although the detector assembly can move to any position inside the mask ($\pm$100 μm), for simplicity, we only allow the assembly to move to the 145 positions shown in Fig. 4. Note that the detector can only move up to 12 cm from the center of the system.

A. Image Reconstruction

We use the following imaging model:

$$\overline{\boldsymbol{y}} = (A\boldsymbol{x} + \boldsymbol{b}) \odot \boldsymbol{t} \tag{1}$$

where $\overline{\boldsymbol{y}}$ is the expected observation vector, A is the system response found using ray tracing [8], [27], $\boldsymbol{x}$ is the image, $\boldsymbol{b}$ is

Authorized licensed use limited to: University of Michigan Library. Downloaded on April 18,2021 at 16:44:55 UTC from IEEE Xplore. Restrictions apply.

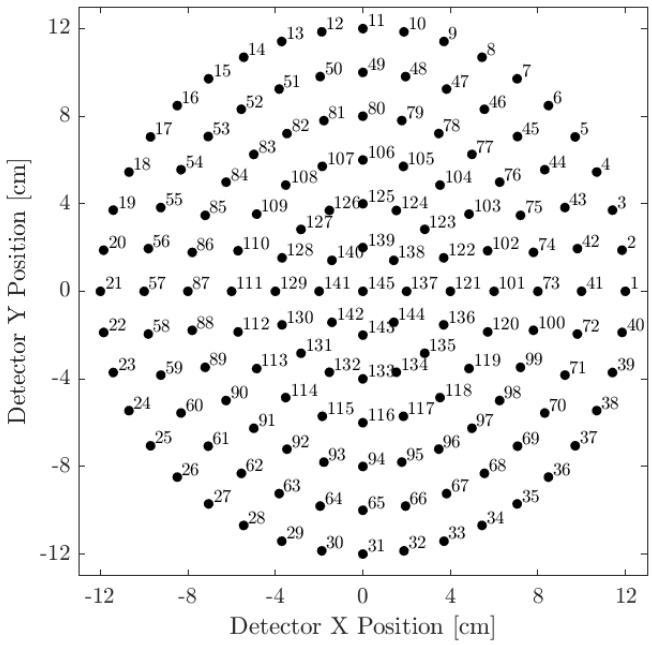

Fig. 4. Candidate detector positions are organized in concentric rings and position numbers are assigned counterclockwise from the outer most ring starting at (12 cm, 0°) and then moving in. Note that there are more candidate detector positions in the outer rings than in the inner ones and position number 145 represents a detector at the center of the mask.

the unmodulated intensity, $\odot$ is element-wise multiplication, and $\boldsymbol{t}$ is the measurement time per bin. The unmodulated component is a result of natural background and source scatter from the mask, environment, and detector. We assume that $\boldsymbol{b}$ is constant as a function of mask rotation angle but may change as a function of detector position. Similarly, $\boldsymbol{t}$ is held constant as a function of mask rotation but may change with detector position.

To reconstruct images, we use maximum likelihood expectation maximization (MLEM) [28]. During image reconstruction, we treat $\boldsymbol{b}$ as another element of $\boldsymbol{x}$ and add response columns (one for each detector position) to A as constant, unmodulated background. We initialize MLEM as

$$\hat{x}_j^0 = \frac{1}{\sum_{i=1}^{N_\mathrm{O}} A_{i,j}} \tag{2}$$

where $\hat{\boldsymbol{x}}^0$ is the initial guess for $\boldsymbol{x}$ and N_O is the number of observations. We terminate MLEM when the normalized root mean squared error (NRMSE) between the observation vector and the forward projection is nearly constant. NRMSE is defined as

$$\mathrm{NRMSE}_k = \sqrt{\frac{\left\|\boldsymbol{y} - \overline{\boldsymbol{y}}^k\right\|_2^2}{\left\|\overline{\boldsymbol{y}}^k\right\|_2^2}} \tag{3}$$

where $\boldsymbol{y}$ is the measured data and $\overline{\boldsymbol{y}}^k$ is the forward projection from the MLEM reconstruction at kth iteration.

III. Setup for the Clairvoyant Analysis

For use in an adaptive imaging algorithm, we need measures for localization precision and angular resolution that are both computationally inexpensive so that they can be evaluated on-the-fly during the planning step and broadly applicable so that they can be used in scenarios with multiple sources of differing relative intensities. Additionally, our interest is not in measuring the absolute performance of the system but rather in measuring the change in performance from repositioning the detector. To that end, this section provides some nomenclature and definitions.

Assume that there are S sources in the FOV and the imaging system has collected full revolutions of data at D detector positions. For each source, there are two model parameters: the intensity of the sth source (α_s) and the azimuthal position of the sth source (ϕ_s). We treat the radial position of all sources as fixed at 90 cm from the center of the mask. Let

1) $\boldsymbol{\alpha}$ be the vector of source intensities: $\boldsymbol{\alpha} = [\alpha_1, \cdots, \alpha_s]^T$;
2) $\boldsymbol{\phi}$ be the vector of azimuthal source positions: $\boldsymbol{\phi} = [\phi_1, \cdots, \phi_s]^T$;
3) $\boldsymbol{\vartheta}_s$ be the parameter vector for the sth source: $\boldsymbol{\vartheta}_s = [\alpha_s,\ \phi_s]^T$; and
4) $\boldsymbol{\vartheta}_S$ be the parameter vector for S sources: $\boldsymbol{\vartheta}_S = [\boldsymbol{\vartheta}_1^T, \cdots, \boldsymbol{\vartheta}_s^T]^T$.

Since data were collected at D detector positions, let $\boldsymbol{b}_D$ be a vector of unmodulated intensities. Thus, there are a total of $(2S + D)$ model parameters: $\boldsymbol{\vartheta} = [\boldsymbol{\vartheta}_S^T,\ \boldsymbol{b}_D^T]^T$. As part of the clairvoyant analysis, we use the true values of $\boldsymbol{\vartheta}$ to measure the localization precision and angular resolution of the different system configurations.

For the clairvoyant analysis, the absolute values of $\boldsymbol{\alpha}$ and $\boldsymbol{b}_D$ are not important, only the relative values are. We define source-to-background ratio (S:B) as the count rate observed from a fully open region of the mask divided by the unmodulated intensity. Thus, we define $\boldsymbol{b}_D$ using a unit value for $\boldsymbol{\alpha}$ and a predefined S:B ratio. Previous experimental work has shown that for a Cf-252 source 90 cm from the system, the S:B ratio is constant at 2.2:1 for all detector positions [27].

A. Measuring Localization Precision and Angular Resolution

Localization precision and angular resolution are distinct but related metrics for an imaging system [29]. Localization precision is the uncertainty when estimating the location of a source, whereas angular resolution is the ability to resolve details in the image, that is, to resolve point sources that are close together. From an information-theoretic perspective, the variance of an unbiased estimate of the location of a source is asymptotically bounded by the Cramér-Rao lower bound (CRLB) [30] (see Appendix A for more details on the CRLB). Thus, we define localization precision as the square root of the CRLB of the source position

$$\sigma_{\phi_s}(\boldsymbol{\vartheta}, A) = \sqrt{\mathrm{CRLB}(\boldsymbol{\vartheta}, A)[I_{\phi_s}, I_{\phi_s}]} \tag{4}$$

where σ_{ϕ_s} is the localization precision of the system for a source at ϕ_s, $\boldsymbol{\vartheta}$ are the true values of the model parameters, and $[I_{\phi_s}, I_{\phi_s}]$ are the indexes of the sth source position (ϕ_s) in $\boldsymbol{\vartheta}$. Note that (4) is a statistical measure in that it accounts for the Poisson nature of the observations and accordingly changes as a function of measured counts, that is, changes

Authorized licensed use limited to: University of Michigan Library. Downloaded on April 18,2021 at 16:44:55 UTC from IEEE Xplore. Restrictions apply.

with the mask design, detector sensitivity, source scene, and measurement time.

There are many methods to measure the angular resolution of a system [31]. One common method uses hypothesis testing to determine whether one or two point sources are present. Under simplifying assumptions, Liu and Nehorai [32] show that the angular resolution limit of a system is asymptotically proportional to $\sqrt{\mathrm{CRLB}[I_{\phi_s}, I_{\phi_s}]}$. Additionally, such a proportional relationship has been assumed by many researchers in varying contexts (see references in [33]). Thus, we define the angular resolution of a system at ϕ_s as directly proportional to the localization precision of the system at ϕ_s

$$\mathrm{AR}_{\phi_s}(\boldsymbol{\vartheta}, A) = \lambda \sigma_{\phi_s} \tag{5}$$

where AR_{ϕ_s} is the angular resolution of the system at ϕ_s, λ is an arbitrary proportionality constant, and σ_{ϕ_s} is the localization precision at ϕ_s. We assume that λ is constant for all detector positions and sources in the FOV. Since (4) and (5) only differ by a proportionality constant, they are equivalent on a relative change basis. Thus, the results in the following sections apply to both localization precision and angular resolution even though they are different performance measures. For ease of reading, the results are interpreted from the perspective of source localization. To interpret the results from the perspective of angular resolution, one can imagine two equal-intensity point sources near ϕ_s instead of one point source at ϕ_s. From this point onward, we refer to both localization precision and angular resolution collectively as performance.

B. One Point Source

To optimize performance when there is one point source in the FOV, we define the objective function (ψ) as

$$\psi(\boldsymbol{\vartheta}, A) = \left(1 - \frac{\sigma_\phi(\boldsymbol{\vartheta}, A)}{\sigma_\phi(\boldsymbol{\vartheta}, A_{D(0,0)})}\right) \tag{6}$$

where ψ is dependent on the model parameters ($\boldsymbol{\vartheta}$), the candidate system response (A), and the system response for the conventional, detector-centered, c-TEI system ($A_{D(0,0)}$).

We refer to (6) as the performance gain. The system response that maximizes the performance gain is

$$A_{\max} = \underset{A \in \mathbb{A}}{\arg\max}\ \psi(\boldsymbol{\vartheta}, A) \tag{7}$$

where $\mathbb{A}$ is the set of system response matrices for each of the 145 candidate detector positions.

C. Multiple Point Sources

When considering multiple point sources, we define the objective ψ as

$$\psi(\boldsymbol{\vartheta}, A) = \left(1 - \frac{U\big(\boldsymbol{\sigma}_{\boldsymbol{\phi}}(\boldsymbol{\vartheta}, A)\big)}{U\big(\boldsymbol{\sigma}_{\boldsymbol{\phi}}(\boldsymbol{\vartheta}, A_{D(0,0)})\big)}\right) \tag{8}$$

where $U(\boldsymbol{\sigma}_{\boldsymbol{\phi}}(\boldsymbol{\vartheta}, A))$ is the quadrature sum of the localization precision for each source

$$U\big(\boldsymbol{\sigma}_{\boldsymbol{\phi}}(\boldsymbol{\vartheta}, A)\big) = \sqrt{\sum_{s=1}^{S} \sigma_{\phi_s}^2(\boldsymbol{\vartheta}, A)}. \tag{9}$$

We refer to (8) as the quadrature-sum performance gain.

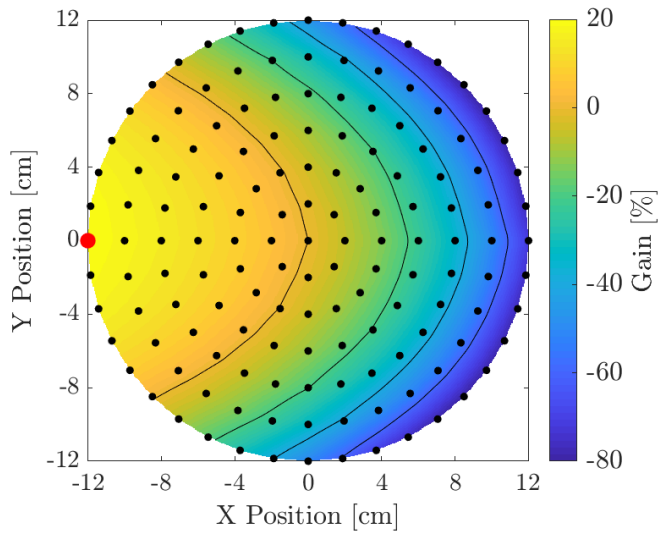

Fig. 5. Performance gain as a function of detector position for one point source centered at (90 cm, 0°). The black dots are the candidate detector positions and the red dot represents the detector position that maximizes the performance gain. The contour lines have the same values as the tick marks on the color bar and the values between detectors positions are interpolated.

D. Two Detector Positions

For all of the scenarios considered here, we also investigate the benefit of combining data from two off-center detector positions instead of just one off-center detector position. In this case, we must optimize over all possible pairs of detector positions and the relative time spent at each position. Let $\boldsymbol{\tau}$ be a vector of D relative measurement times. Then, the candidate system response for two detector positions is

$$A = [\tau_1 A_{D_1}^T \ \ \tau_2 A_{D_2}^T] \tag{10}$$

where A_{D_d} is the system response for the dth detector position and τ_d is a fraction of the total measurement time. The two detector position optimization problem is

$$A_{\max} = \underset{\substack{A_{D_1},\ A_{D_2} \in \mathbb{A} \\ \sum_{d=1}^{D} \tau_d = 1}}{\arg\max}\ \psi(\boldsymbol{\vartheta}, A). \tag{11}$$

For simplicity, we constrain τ_d to discrete values ranging from 10% to 90% every 10%. All optimizations were done by exhaustive search.

IV. One Point Source

We start with the simplest case of one point source at (90 cm, 0°). Fig. 5 shows the performance gain (6), predicted by the clairvoyant analysis as a function of detector position. As one would expect, the gain is maximized at (12 cm, 180°) which is the detector position that maximizes the detector-to-mask distance away from the source. The clairvoyant analysis predicts that repositioning the detector provides 20% better performance compared to the conventional case. On the other hand, if the detector position is poorly chosen, the performance loss can be up to 80%.

This effect is also evident in Fig. 6 which maps the performance gain as a function of source position for a fixed detector at (6 cm, 180°) or (12 cm, 180°). Observe that as

Authorized licensed use limited to: University of Michigan Library. Downloaded on April 18,2021 at 16:44:55 UTC from IEEE Xplore. Restrictions apply.

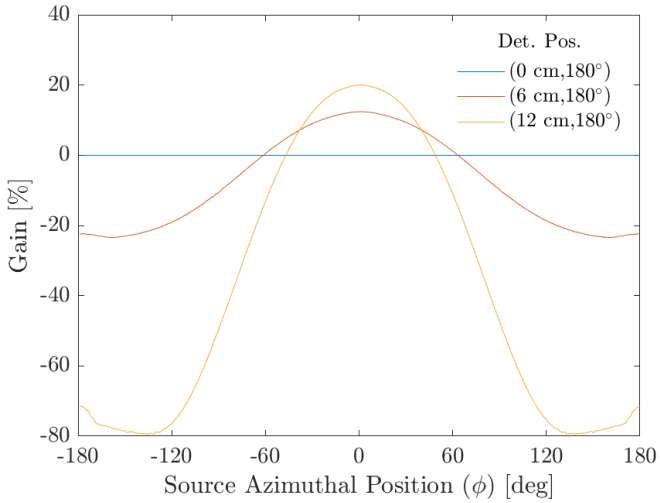

Fig. 6. Performance gain as a function of source position for three detector positions.

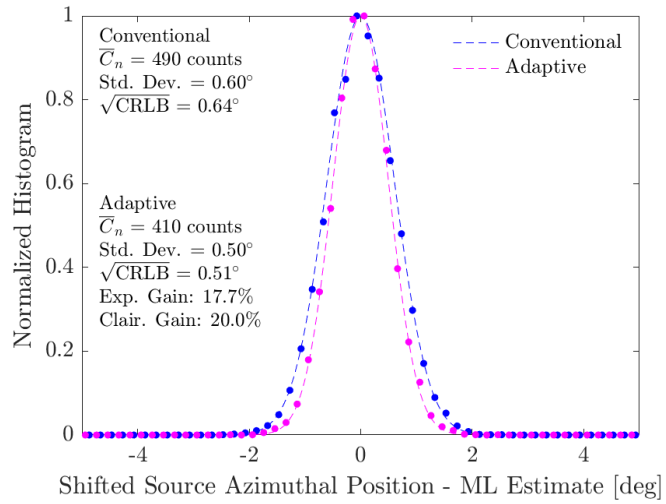

Fig. 7. Normalized and shifted histograms of $\hat{\phi}_{\text{ML}}$ created from 10 000 replicates of experimental data. The source is at (90 cm, 178°) and the clairvoyant adaptive case uses data collected at (12 cm, 0°). The dashed lines represent a Gaussian fit and the dots are the bin centers of the histogram.

the detector moves further off-center, the performance gain increases but the region of improved performance decreases. At the furthest off-center position, performance only improves for sources that are <50° of the imaging axis. Additionally, there is only significant gain (>15%) within ±25° of the imaging axis.

A. Experimental Verification

We experimentally verify these results in two ways. First, we verify that the localization precision of the system improves by creating a histogram of source position maximum likelihood estimate (MLE) ($\hat{\phi}_{\text{ML}}$) for both cases and comparing the standard deviations of the histograms. Since the maximum likelihood (ML) solution is asymptotically unbiased and asymptotically efficient [30], the MLE distributions also serve as a verification of the CRLB calculation. Second, we qualitatively verify that the angular resolution improves by reconstructing images of two equal-intensity point sources that are close together.

For the localization precision verification, we use fast-neutron data from a 1.85 mCi Cf-252 source placed at (90 cm, 178°) and measured for 90 s. The conventional case uses data collected when the detector was at the center of the mask and the clairvoyant adaptive case uses data collected when the detector was at (12 cm, 0°). To make the $\hat{\phi}_{\text{ML}}$ histograms, we create 10 000 replicates of the experimental data as if the source was 1% the original source strength and estimate $\hat{\phi}_{\text{ML}}$ for each replicate. Fig. 7 shows the resulting histograms for both cases. Based on the Gaussian fits, the standard deviation of the histogram from the clairvoyant adaptive case is 17.7% narrower than the conventional case. This result is in line with the prediction from the clairvoyant analysis (Fig. 5).

For the angular resolution verification, we combine fast-neutron data from two sequential measurements. In the first measurement, a 1.85 mCi Cf-252 source was placed at (90 cm, 175°) and in the second, the same source was placed at (90 cm, 185°). Data were collected at each off-center detector position in Fig. 4 for 90 s. For the conventional case reconstructions, we use 90 s of data when the detector was centered, and for the clairvoyant adaptive case, we use 90 s of data when the detector was at (12 cm, 0°).

Fig. 8(a) and (b) shows the two-source MLEM reconstructions under the conventional and clairvoyant adaptive cases. In the conventional case, the two sources are not resolved after 75 iterations, whereas in the clairvoyant adaptive case, the two sources are clearly resolved. These verifications provide confidence that the performance gains predicted by the clairvoyant analysis are experimentally achievable if the source scene is known beforehand. The experiments show that collecting data at the optimal off-center detector position improves both the localization precision and the angular resolution of the system.

B. Generalizing to Other c-TEI Systems

Thus far, we have shown the performance gain from collecting data at one off-center detector position for sources that are along the imaging axis and 90 cm from the MATADOR system. This section generalizes the results to any detector offset and radial position of the source using a geometric measure for angular resolution gain.

As discussed earlier, two sources are deemed to be resolvable if they are separated by the angular width of a unit mask element. As shown in Fig. 1, repositioning the detector decreases the angular separation at which two sources are separated by a unit mask element. We define the geometric angular resolution gain as

$$\text{AR}_{\text{G}} = 1 - \frac{\theta_{\text{o}}}{\theta_{\text{c}}} \tag{12}$$

where AR_{G} is the geometric angular resolution gain and θ_{o} and θ_{c} are defined in Fig. 1. Additionally, the detector offset (d), the mask radius (r_{m}), and the radial position of the source (r_s) are shown in Fig. 1 as well.

Authorized licensed use limited to: University of Michigan Library. Downloaded on April 18,2021 at 16:44:55 UTC from IEEE Xplore. Restrictions apply.

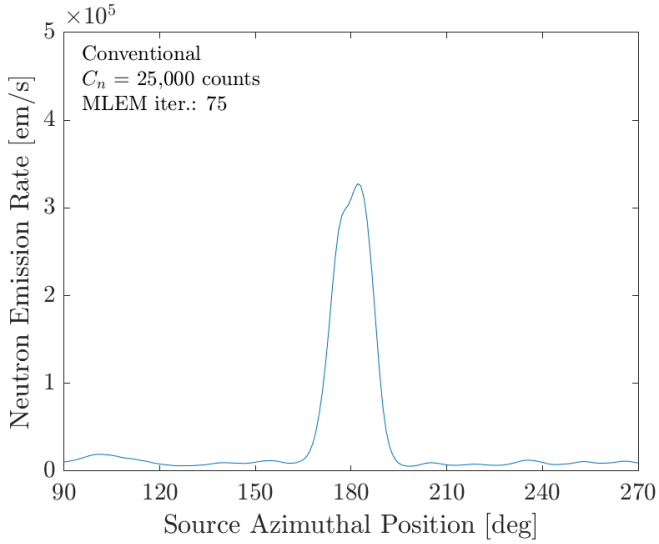

(a)

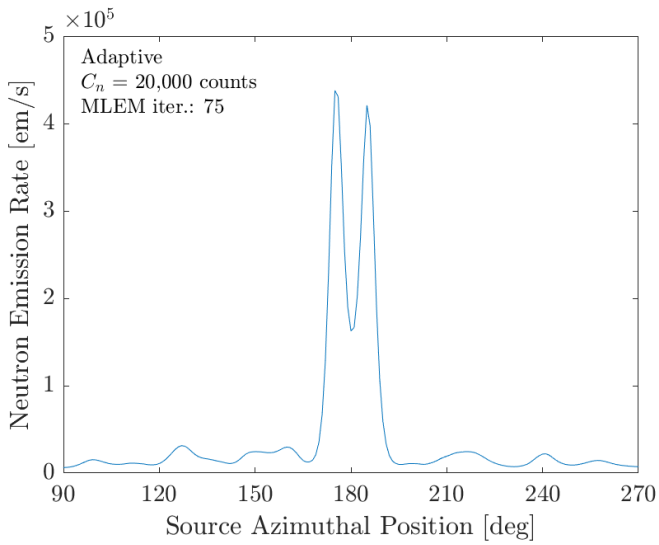

(b)

Fig. 8. Reconstructed images of two point sources at (90 cm, 175°) and (90 cm, 185°). (a) Conventional c-TEI reconstruction. (b) Clairvoyant adaptive c-TEI reconstruction with the detector at (12 cm, 0°).

Fig. 9 plots the geometric gain as a function of the relative radial position of the source (r_s/r_m) and the relative detector offset (d/r_m). For r_m, we use the outer mask radius. Notice that as the source moves from the near-field to the far-field, the gain increases. Additionally, as the relative detector offset increases, the gain increases. All of the experiments in this article were conducted at a relative radial position of 90 cm/25.7 cm = 3.5. Since MATADOR has a thick mask and a large detector, the detector cannot physically move to r_m. The maximum relative detector offset for MATADOR is 12 cm/25.7 cm = 0.47. The geometric gain for the MATADOR system (red dashed line) shows good agreement with the performance gain calculated using the CRLB (solid red line). For a far-field source, the maximum geometric angular resolution gain for the MATADOR system is ∼32%. In contrast, an ideal system

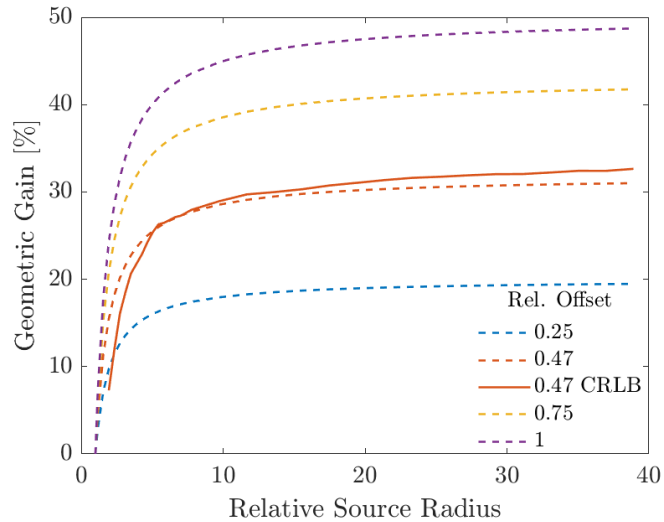

Fig. 9. Geometric angular resolution gain as a function of the relative radial position of the source (r_s/r_m) and the relative detector offset (d/r_m).

with a thin mask and a point detector has a maximum gain of 50% since the detector can reach a larger relative offset.

V. Two Point Sources

The previous section shows that adaptive detector movements can improve performance for one point source but only for a limited FOV. Sources that are not within that FOV will suffer from worse performance. This section extends the clairvoyant analysis to two point sources as a function of the angular separation between the sources and their relative intensity. We use (8) to measure the quadrature-sum performance gain.

To map performance gain as a function of source separation and relative intensity, we simulate separations of 2° to 180° every 2° and vary the intensity ratios (α_1:α_2) of the sources from equal intensity (5:5) to a large relative intensity differences (9:1). For each case, we find the detector position that maximizes (8) and record the quadrature-sum performance gain. Fig. 10 shows the corresponding plot. Although performance gain is a complex function of source separation and relative intensity, Fig. 10 can be understood by considering the optimal detector position for each source and the optimal detector position based on the quadrature-sum performance gain.

For each source, there exists a detector position that maximizes performance. When two sources are close together (<20°), their respective optimal detector positions are also close together. Thus, one detector position can maximize the performance for each source regardless of their relative intensity. This results in high quadrature-sum performance gain at small source separations as demonstrated in Fig. 10. Note that the maximum gain is ∼50% which is significantly larger than the ∼20% gain in the one-source case. From an estimation perspective, the greater the similarity between the responses from two sources, the more difficult it is to precisely estimate their positions. Repositioning the detector

Authorized licensed use limited to: University of Michigan Library. Downloaded on April 18,2021 at 16:44:55 UTC from IEEE Xplore. Restrictions apply.

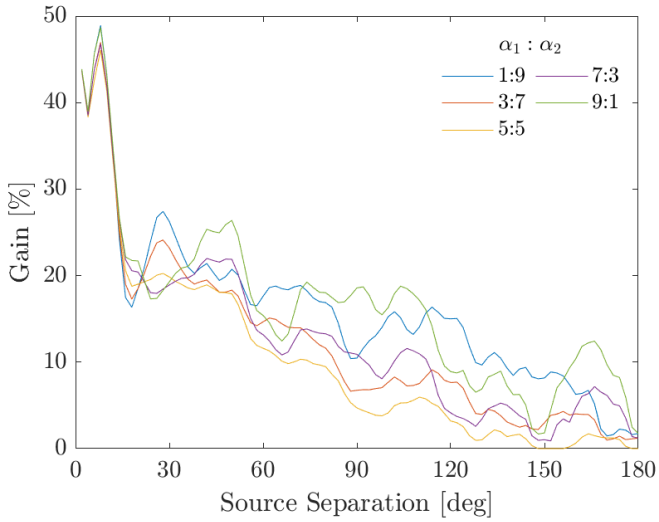

Fig. 10. Quadrature-sum performance gain using one off-center detector position for two point sources as a function of source separation and relative intensity.

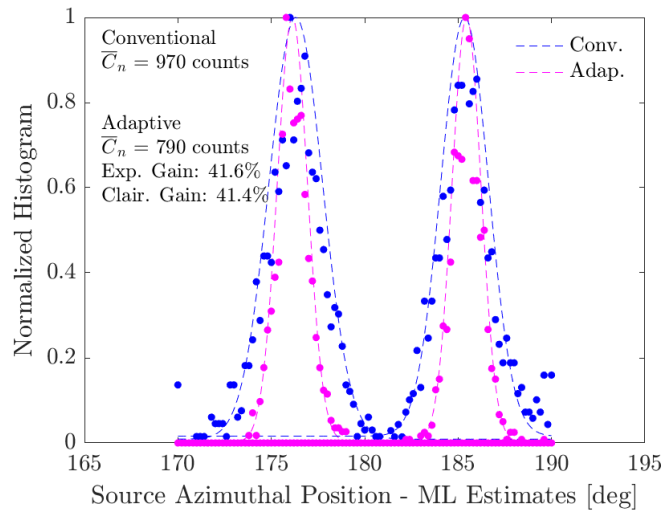

Fig. 11. Histograms of $\phi_{1,\mathrm{ML}}$ and $\phi_{2,\mathrm{ML}}$ from both the conventional and clairvoyant adaptive cases. The clairvoyant adaptive case uses data collected at (12 cm, 0°). The sources are at (90 cm, 175°) and (90 cm, 185°). The dashed lines represent Gaussian fits and the dots are the bin centers of the histogram.

from the center to the optimal position has the dual effect of reducing the similarity between ϕ_1 (or ϕ_2) and its nearby neighbors and reducing the similarity between ϕ_1 and ϕ_2. Thus, the quadrature-sum gain is greater when there are multiple sources that are close together than if there is only one source. Note that even though the performance gain from repositioning the detector is greater in the two-source case compared to the one-source case, in absolute terms, the performance is worse because more parameters must be estimated from a similar set of observations.

If two sources are far apart, then the optimal detector positions for each source are also far apart. This results in a lower quadrature-sum performance gain since the detector position that maximizes performance for one source results in poor performance for the other (recall Fig. 6). If the two sources have equal intensity, then the system must select a detector position that compromises between the performance for each source.

On the other hand, if there are large intensity differences between the sources, then the performance of the low-intensity source dominates the quadrature-sum gain. In this case, the system can select a detector position that achieves the maximum gain for the weaker source without considering the performance loss of the stronger source. Thus, the gain increases as the relative difference in intensities increases.

Also evident from Fig. 10 is that the performance gain is greatest when the two sources are 8° apart. Intuitively, one would expect a separation of ∼10° to lead to the greatest performance gain. Recall from Section II that in the MATADOR system, mask elements are ∼10.3° wide. Thus, in an ideal system (i.e., point detector, thin masks, and far-field sources), if two sources are separated by ∼10.3°, then they are likely to experience mask element transitions at the same mask rotation angle. These overlapping transitions make localization of the two sources more difficult than if the sources were separated by a greater or lesser amount. At the optimal detector position, the expected responses from the two sources change such that the two responses do not have overlapping mask element transitions, and the performance gain improves dramatically. The difference between our intuition and the observation in Fig. 10 may be the result of the nonideal (i.e., large detector, thick masks, and near-field sources) scenarios studied here, although more work is necessary to fully understand the result.

A. Experimental Verification

Similar to the one-source case, we experimentally verify these results through MLE of the source positions and MLEM reconstruction. For the localization precision verification, we use data from the two-source setup described in Section IV-A. We create 1000 replicates of the experimental data as if the sources were 1% of their original strengths and estimate $\phi_{1,\mathrm{ML}}$ and $\phi_{2,\mathrm{ML}}$ for each replicate. Fig. 11 shows the resulting histograms for both sources and both cases. Using the quadrature sum of the standard deviations of the Gaussian fits, the gain is ∼42%, in line with the prediction from the clairvoyant analysis for equal-intensity point sources.

For the angular resolution verification, we reconstruct images of two pairs of two point sources that are 10° apart. The first pair of sources is centered at 153° and the second is centered at 207°. We synthetically create this data by using data from the two measurements described in Section IV-A. See Appendix B for more details on this process.

Fig. 12 shows the four-point source reconstruction in the conventional and clairvoyant adaptive cases. When the detector is centered, neither pair of point sources can be separated, whereas when the detector is at (12 cm, 0°), all four sources are clearly resolved. These experiments show that the performance gains predicted by the clairvoyant analysis can be experimentally realized.

Authorized licensed use limited to: University of Michigan Library. Downloaded on April 18,2021 at 16:44:55 UTC from IEEE Xplore. Restrictions apply.

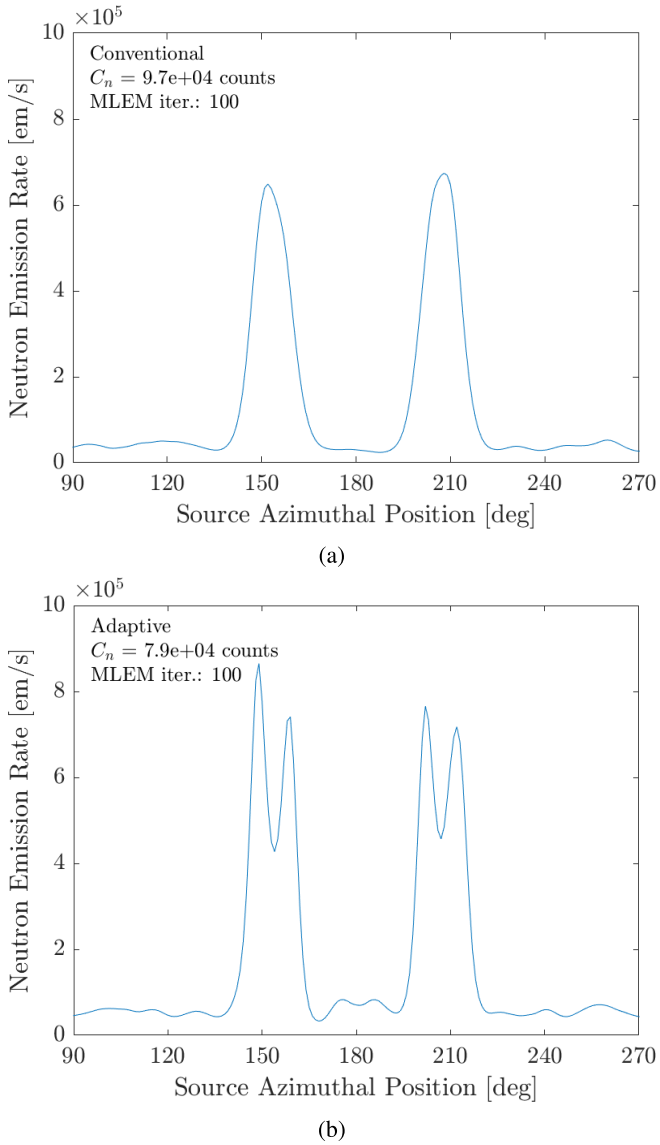

Fig. 12. Reconstructed images of two pairs of two point sources that are 10° apart. The first pair of sources is centered at 153° and the second is centered at 207°. (a) Conventional c-TEI reconstruction. (b) Clairvoyant adaptive c-TEI reconstruction with the detector at (12 cm, 0°).

VI. Two off-Center Detector Positions

Sections IV and V presented the benefit of collecting data at one off-center detector position, but it may be possible to achieve better performance by combining data from multiple off-center detector positions. We explore this idea by using (11) and finding the performance gain when combining data from two off-center detector positions. Section VI-A considers the case of one point source and Section VI-B considers the case of two point sources in the FOV.

A. One Point Source

Assuming there is a point source at (90 cm, 0°), Fig. 13 plots the performance gain as a function of the first and second detector positions identified by the position number, as shown in Fig. 4. The relative measurement time between the detector positions is coarsely optimized for each pair and only the gain from the optimal $\boldsymbol{\tau}$ is shown. The red dot represents the pair of detectors that lead to the greatest performance gain. The conventional case is the top right corner at index (145, 145). Any point along the diagonal from the bottom left to the top right is equivalent to collecting data at one detector position for the entire measurement time. Extracting the diagonal elements and plotting them by their x, y detector positions would recreate Fig. 5.

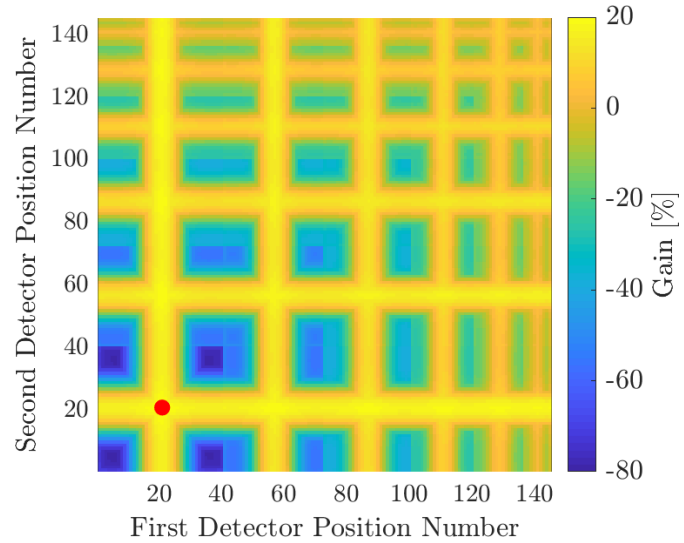

Fig. 13. Performance gain when combining data from two off-center detector positions for one point source at (90 cm, 0°). The relative measurement time between the detector positions is coarsely optimized for each pair and only the gain from the optimal $\boldsymbol{\tau}$ is shown. Recall that position numbers are assigned counterclockwise from the outer most ring starting at (12 cm, 0°) and then moving in. Note that there are more candidate detector positions in the outer rings than in the inner ones and position number 145 represents a detector at the center of the mask.

Recall from Fig. 5 that for a point source at (90 cm, 0°), the optimal detector position is (12 cm, 180°) which corresponds to detector position number 21 in Fig. 4. As shown in Fig. 13, the optimal pair of detectors is (21, 21), that is, collecting data at the same detector position twice. Thus, there is no added benefit to collecting data at two off-center detector positions relative to the best off-center detector position for a single point source.

B. Two Point Sources

If there are two sources present, perhaps combining data from two off-center detector positions, such as the optimal detector position for each source, will lead to better performance than only using data from the compromise position. Fig. 14 plots the quadrature-sum performance gain from the optimal pair of detector positions as a function of source separation and relative intensity and Fig. 15 plots the absolute difference in gain between the two detector position (Fig. 14) and one detector position (Fig. 10) results. Note that the results in Figs. 10 and 14 are quite similar and thus the absolute difference shown in Fig. 15 is small.

Looking at Fig. 15, it is evident that for many of the scenarios considered here, there is no benefit to combining

Authorized licensed use limited to: University of Michigan Library. Downloaded on April 18,2021 at 16:44:55 UTC from IEEE Xplore. Restrictions apply.

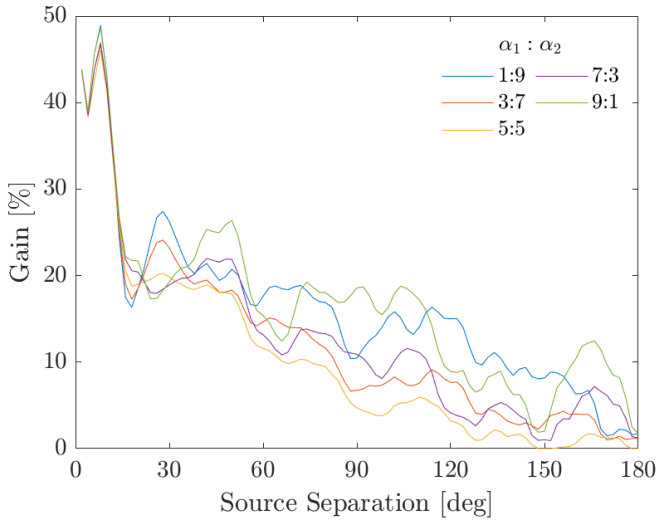

Fig. 14. Quadrature-sum performance gain using two off-center detector positions for two sources as a function of source separation and relative intensity.

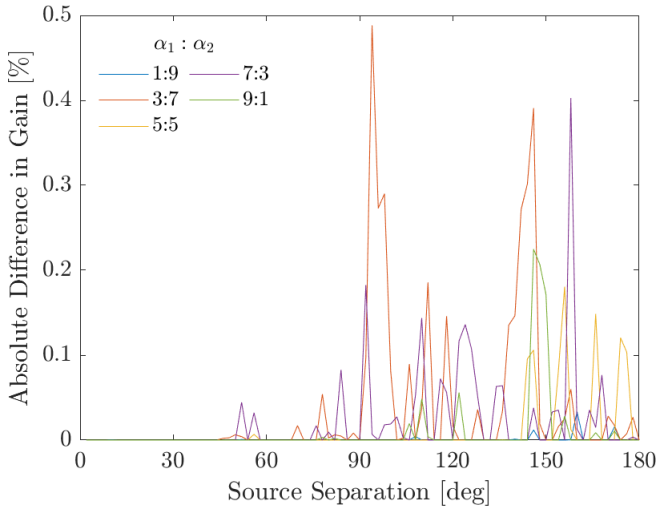

Fig. 15. Absolute difference in performance gain between two off-center detector positions and one off-center position as a function of source separation and relative intensity.

data from two off-center detector positions relative to using data from one off-center detector position. In select cases, there is some benefit, but it is small and not worth the time spent moving the detector to two positions instead of one. We attribute these results to the observation that collecting higher quality data for one source often means collecting significantly lower quality data for the other source.

In both the one-point source and two-point source scenarios, we find that there is little to no benefit in collecting data at two off-center detector positions compared to one off-center detector position. Thus, when improving localization precision and angular resolution, we conclude that collecting data at multiple off-center detector positions is not valuable for sources that are fixed at 90 cm. Instead, the detector should spend all of the available measurement time at one optimal

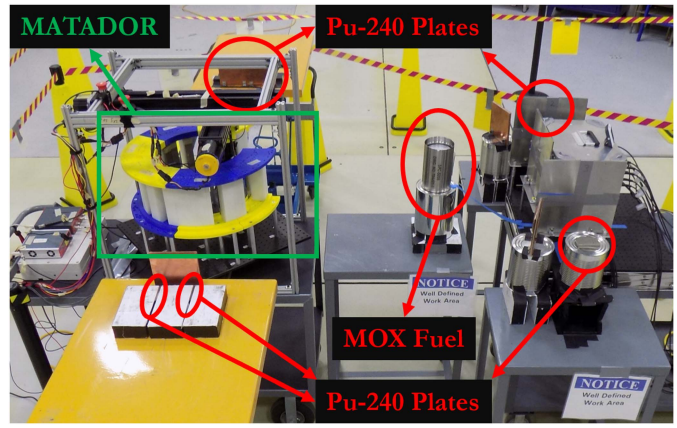

Fig. 16. Photograph of the multiple source measurement at the ZPPR facility at INL.

off-center position. Note that this result assumes that the radial position of the source is fixed at 90 cm. If the radial position must also be estimated, multiple detector positions may offer a benefit, but we have not explored this.

VII. Demonstration With a Complex Arrangement of Special Nuclear Material

To demonstrate the value of adaptive detector movements in a complex scenario, we set up a multiple source experiment at the ZPPR facility at INL using special nuclear material. The setup includes five radioactive objects made using metallic plutonium plates with a high concentration of Pu-240 and mixed oxide (MOX) fuel pins. They are of varying intensity at different radial distances from the system. Fig. 16 shows a photograph of the setup and Fig. 17 shows the setup in (r, θ) coordinates; a detailed description of the setup is given in Appendix C.

For this demonstration, we focus on reconstructing the two sources centered at (80 cm, 90°) which are two equal-intensity point-like sources that are 8° apart. The two sources are significantly weaker in intensity than the MOX fuel at 180°, thus this is a challenging imaging scenario. Since the objects are distributed in (r, θ), we reconstruct the images in 2-D polar coordinates.

Hypothetically, a nonclairvoyant adaptive imaging algorithm would start by collecting data with the detector centered and use that data to estimate $\boldsymbol{\vartheta}$. Then, the remaining measurement time would be spent at the optimal off-center detector position. We cannot implement such an algorithm for the multiple source experiment because of insufficient counts at the off-center detector positions. At ZPPR, we collected data with the detector at the center for 24 revolutions (36 min) and with the detector at each of the 144 off-center positions denoted in Fig. 4 for one revolution (90 s) each. There is not enough data at a single off-center detector position to adequately reconstruct an image. Thus, for the adaptive case in this demonstration, we combine data from multiple off-center detector positions. The adaptive reconstructions use three revolutions of data with the detector at the center and one revolution of data from the 21 off-center detector positions

Authorized licensed use limited to: University of Michigan Library. Downloaded on April 18,2021 at 16:44:55 UTC from IEEE Xplore. Restrictions apply.

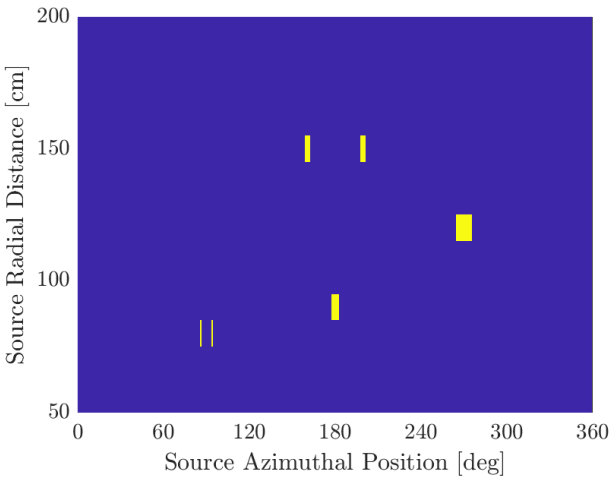

Fig. 17. Two-dimensional polar representation of the multiple source measurement.

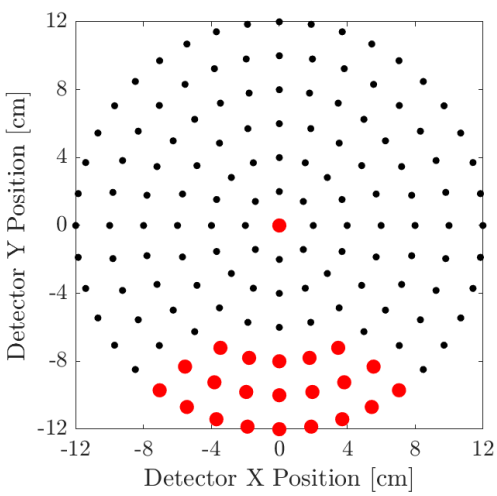

Fig. 18. Red dots represent the detector positions used for the adaptive reconstructions in the multiple source experiment.

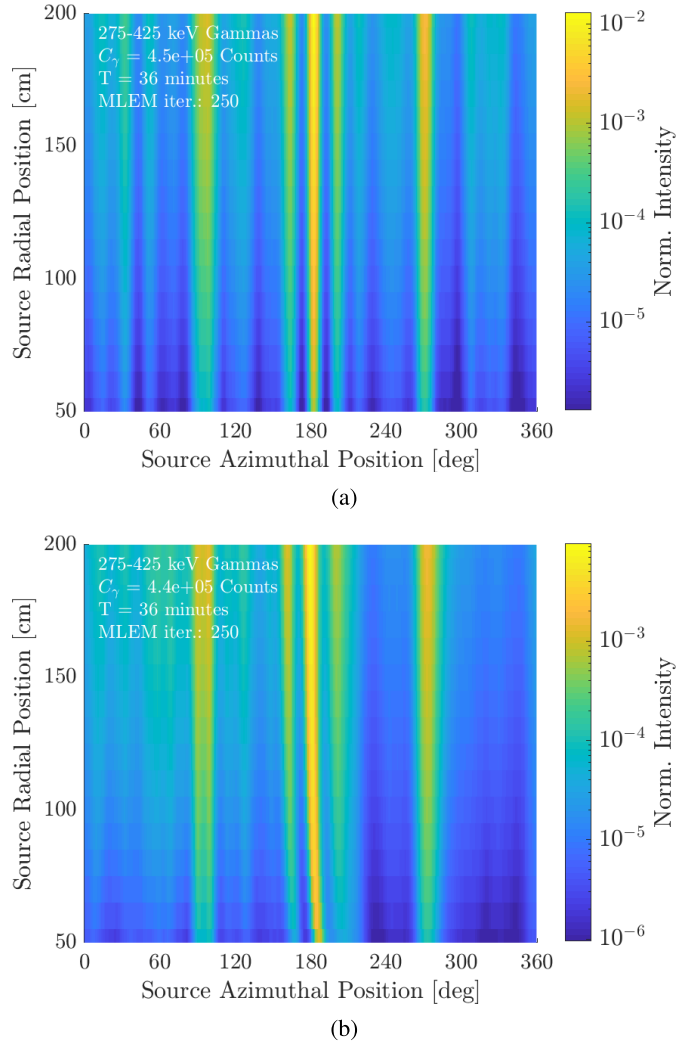

Fig. 19. Two-dimensional gamma-ray reconstructions of the multiple source experiment. (a) Conventional case using 24 revolutions of data with the detector at the center. (b) Adaptive case using three revolutions of data with the detector at the center and one revolution of data at each of the 21 off-center detector positions highlighted in Fig. 18.

highlighted in red in Fig. 18. The conventional case uses a time-equivalent 24 revolutions of data with the detector centered. To combine data from multiple revolutions at the same detector position, we sum the observed counts for each mask rotation angle, and to combine data from different detector positions, we concatenate the observation vectors. The response matrices are scaled and concatenated accordingly.

Although both fast-neutron and gamma-ray data were collected using the stilbene and CLLBC detectors, this section only presents gamma-ray reconstructions using the CLLBC detector. The reconstructions use interactions that deposited between 275 and 425 keV; a sample energy spectra is shown in Appendix C.

Fig. 19 shows 2-D reconstructions for both the conventional and adaptive cases, and Fig. 20 shows the radial slices at 80 cm. In Fig. 20, notice that the two sources at 90° cannot be resolved when the detector is at the center, but when we utilize data from off-center detector positions, the two sources are clearly resolved. Thus, even in a challenging scenario with significantly stronger sources in the FOV, repositioning the detector improves angular resolution. One should note though that the performance for sources significantly off-axis from the imaging axis, such as the object at 200°, may be worse in the adaptive case than the conventional. Thus, the user must decide which objects are important to capitalize on the source localization and angular resolution advantages.

VIII. Discussion

These results show that adaptive detector movements can improve the localization precision and angular resolution of c-TEI systems, but there are some important limitations to consider. First, the performance of the system does not improve uniformly throughout the FOV. If a source is far from the imaging axis, the performance can be significantly worse for an off-center detector than for a centered detector. If there is one source in the FOV or multiple sources that are close together, this limitation is irrelevant since an adaptive imaging

Authorized licensed use limited to: University of Michigan Library. Downloaded on April 18,2021 at 16:44:55 UTC from IEEE Xplore. Restrictions apply.

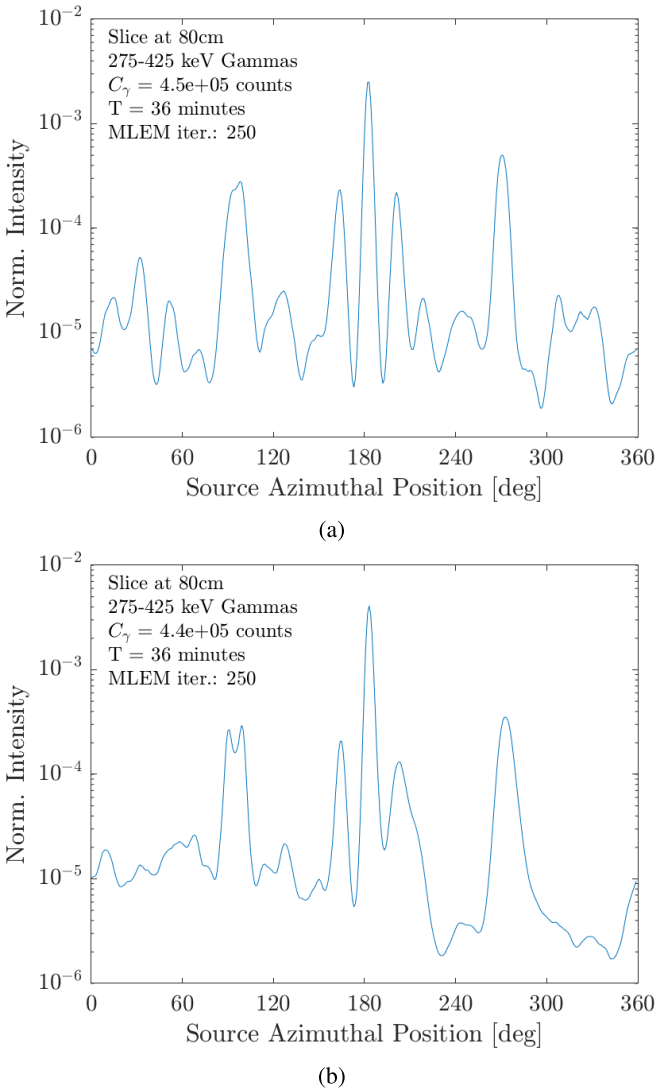

Fig. 20. Radial slices at 80 cm from 2-D reconstructed images of the multiple source experiment. Observe that the two point sources centered at 90° cannot be separated in the conventional case but are separated in the adaptive case. (a) Conventional case. (b) Adaptive case.

algorithm can simply move the detector to the position that achieves good performance for all sources. But if there are multiple sources that are spread out in the FOV, then improving performance with respect to one source inherently results in worse performance for the others. This limits the performance gain from adaptive detector movements. Of course, an adaptive c-TEI system will always outperform a conventional c-TEI, but in some cases, the performance gain is not significant.

One might attempt to overcome this limitation by combining data from multiple off-center detector positions, such as collecting data at the optimal detector positions for each source. We implemented this concept for sources that are fixed at 90 cm from the system and find that combining data from two off-center detector positions does not significantly improve performance compared to collecting data at the one off-center detector position. Note that the value of combining data from multiple detector positions may change if the radial position of the source must be estimated.

The maximum performance gain from adaptive detector movements is also strongly dependent on the relative offset and the relative radial position of the source. Fundamentally, the performance gain of an ideal, adaptive c-TEI system for one far-field point source is limited to 50%, but since the MATADOR system utilizes a thick mask and a large detector to image fast neutrons, it cannot reach that limit. On the other hand, if one is implementing adaptive detector movements on a system with relatively thin masks and a small detector, such as a high-resolution gamma-ray system, the performance gain would be closer to the limit. Additionally, the relative radial position of the source also plays an important role in performance gain. Near-field sources experience significantly smaller performance gains than far-field sources. Thus, it is important to consider the expected radial positions of the sources when designing an adaptive c-TEI system.

Finally, the results presented here are based on a clairvoyant analysis where all of the model parameters, such as the strength and position of the sources, are known beforehand. In the real-world, one must use collected data to estimate the unknown parameters. This will lead to worse performance as time is spent at nonoptimal detector positions before the parameters can be estimated. Moreover, parameter estimation introduces uncertainty, particularly in low-count scenarios, which can result in collecting data at nonoptimal detector positions. This may limit the achievable gain from adaptive detector movements and must be considered when implementing an adaptive algorithm.

In spite of these limitations, adaptive detector movements have the potential to improve the localization precision and angular resolution of a c-TEI system without increasing the mask radius or reducing the detector size. The improved performance also translates to a shorter time-to-image. Sinclair *et al.* [34] define time-to-image for a gamma-ray imager as the measurement time required to achieve a root-mean-squared error (RMSE) of 2° for a 1 mCi Cs-137 placed 1000 cm from the system. To find the time to image for a fast neutron imager, we use a similar definition except the source is a 1 mCi Cf-252 source instead of a 1 mCi Cs-137 source. We simulated Poisson replicates of the expected observation vector as a function of measurement time and estimated the source position using ML. We assume that one, full revolution of data is collected with an S:B ratio of 2.2:1. Fig. 21 shows the RMSE as a function of measurement time.

When the detector is centered, the time to image is 110.0 s, and when the detector is at the optimal detector position, the time to image is 100.3 s, which is a reduction of 8.8%. Notice though that if the time to image is defined differently, the reduction in the time to image changes. For example, the time to reach an RMSE of 0.7° is 266.8 s in the centered case and 127.0 s in the off-center detector case, which is a reduction of 54.4%. The reduction in the time to image is relatively constant for RMSEs below 0.7° and approaches the asymptotic reduction predicted by the CRLB which is 56.4%.

These benefits from adaptive detector movements come at a relatively small increase in cost and complexity. The addition

Authorized licensed use limited to: University of Michigan Library. Downloaded on April 18,2021 at 16:44:55 UTC from IEEE Xplore. Restrictions apply.

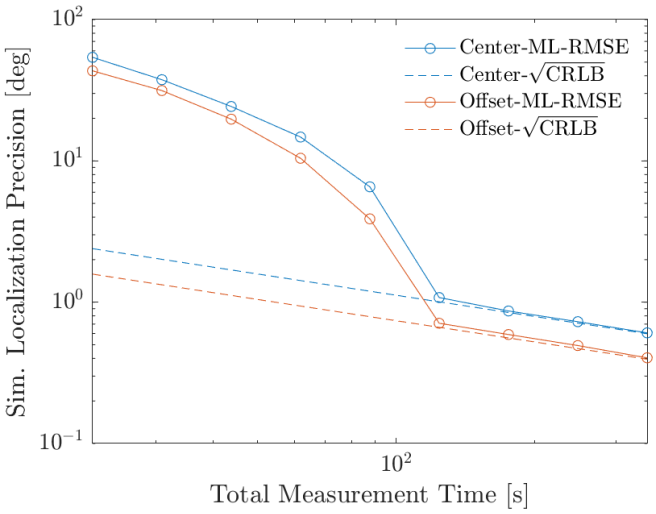

Fig. 21. Simulated localization precision as a function of measurement time for the MATADOR system imaging fast neutrons from a 1 mCi Cf-252 source at (1000 cm, 180°). The S:B ratio is assumed to be 2.2:1. In the off-center case, the detector is at (12 cm, 0°).

of an x–y linear stage to move the detector is straightforward and one can imagine a simple adaptive algorithm, such as the one used in Section VII, where the system collects data with the detector at the center for a predefined period of time, requests user input to define regions of interest, and then repositions the detector accordingly. The low cost and complexity of adaptive detector movements make them an attractive option to improve the localization precision and angular resolution of c-TEI systems.

IX. Conclusion

This article demonstrates the value of adaptive detector movements in improving localization precision and angular resolution of a c-TEI system. When one point source is present, the performance improves by 20% for a source at 90 cm and 32% for a far-field source. When two point sources are present, the performance improves by up to 50% depending on the source separation and relative intensity. If the two sources are close together ($<20°$), then regardless of their relative intensity, the gain is large ($>20\%$). If the two sources are far apart, then gain changes as a function of relative intensity. For sources with large differences in intensity, the gain is $>10\%$ for almost all separations. On the other hand, if the two sources are equal in intensity, then the gain is less than 10% for separations $>75°$.

We experimentally verified these results by both comparing histograms of MLEs of the source position and by reconstructing images using MLEM. For one point source, the histogram under the adaptive case is 17.7% narrower than the conventional, and for two point sources, the quadrature sum of the standard deviations is 42% lower. Both these results are in line with the clairvoyant analysis. The reconstructed images also show clear performance improvements in resolving point sources that are close together. For example, in the conventional case, two point sources that are 10° apart cannot be resolved, whereas in the clairvoyant adaptive case, they are clearly resolved.

We also investigated the value of combining data from two off-center detector positions relative to one off-center detector positions. We find that it does not appreciably improve performance. This result was true for both one and two sources regardless of their separation and relative intensity. This indicates that the focus of an adaptive imaging algorithm tasked with improving localization precision and angular resolution should be on finding the single optimal detector position and not a combination of detector positions. Note that these results assume the sources are fixed at 90 cm from the system. If the radial position of the source must be estimated, the value of adaptive detector movements on localization precision and angular resolution may change.

Section VII demonstrated a hypothetical adaptive imaging algorithm applied to a complex arrangement of special nuclear material. We showed that utilizing data from off-center detectors can improve the angular resolution of the system even when there are multiple sources in the FOV and one source is an order of magnitude more intense than the others.

Given that adaptive detector movements can improve localization precision and angular resolution for a known source scene, the next step is to develop adaptive algorithms that can detect and estimate an unknown source scene. To achieve the maximum benefit from adaptive detector movements, such a detection algorithm must accurately estimate the source scene with low-count data. Additionally, this work focuses on point sources, but a natural extension is to investigate the potential of adaptive detector movements on imaging extended sources. When measuring the width of an extended source, we expect the improved angular resolution to result in lower uncertainty in the estimates. On the other hand, if the application is to map the spatially varying emission intensity of an object, then the results from this article are less applicable and more work is needed to understand the impact of adaptive imaging.

Finally, this article uses adaptive detector movements to improve two general performance measures instead of directly improving performance for a specific application. For example, one could design dedicated algorithms to quantify the fissile mass of a specific object or verify the presence of specific sources. These are good concepts to test in future work.

Appendix A
Cramér-Rao Lower Bound

CRLB is the lower bound on the variance for all unbiased estimators of a deterministic parameter [30]. For example, say we are interested in estimating the background count rate. In this case, one may use some unbiased estimator such as the mean counts measured in a time interval. The variance in this estimator must be greater than or equal to the CRLB. In the context of source localization, the CRLB is the lowest variance on the source position when using any unbiased estimator. Before we introduce the CRLB, we first introduce some relevant variables.

Recall that $\boldsymbol{\vartheta}$ is a vector of model parameters for S sources. Let the gradient, $\nabla_{\boldsymbol{\vartheta}} f(\boldsymbol{\vartheta})$, and the Hessian matrix, $\nabla_{\boldsymbol{\vartheta}} \nabla_{\boldsymbol{\vartheta}}^T f(\boldsymbol{\vartheta})$,

Authorized licensed use limited to: University of Michigan Library. Downloaded on April 18,2021 at 16:44:55 UTC from IEEE Xplore. Restrictions apply.

be defined as

$$\nabla_{\boldsymbol{\vartheta}} f(\boldsymbol{\vartheta}) = \left[\frac{\partial f}{\partial \vartheta_1} \cdots \frac{\partial f}{\partial \vartheta_N}\right]^T$$

$$\nabla_{\boldsymbol{\vartheta}} \nabla_{\boldsymbol{\vartheta}}^T f(\boldsymbol{\vartheta}) = \begin{bmatrix} \frac{\partial^2 f}{\partial \vartheta_1^2} & \frac{\partial^2 f}{\partial \vartheta_1 \partial \vartheta_2} & \cdots & \frac{\partial^2 f}{\partial \vartheta_1 \partial \vartheta_N} \\ \frac{\partial^2 f}{\partial \vartheta_2 \partial \vartheta_1} & \frac{\partial^2 f}{\partial \vartheta_2^2} & & \frac{\partial^2 f}{\partial \vartheta_2 \partial \vartheta_N} \\ \vdots & & \ddots & \vdots \\ \frac{\partial^2 f}{\partial \vartheta_N \partial \vartheta_1} & \frac{\partial^2 f}{\partial \vartheta_N \partial \vartheta_2} & \cdots & \frac{\partial^2 f}{\partial \vartheta_N^2} \end{bmatrix} \quad (13)$$

where $(\partial f / \partial \vartheta_i)$ is the partial derivative of f with respect to ϑ_i.

Given these definitions, the Fisher information matrix (FIM) is

$$I(\boldsymbol{\vartheta}) = -\mathbb{E}\left[(\nabla_{\boldsymbol{\vartheta}}\ \ell(\boldsymbol{y} \mid \boldsymbol{\vartheta}))(\nabla_{\boldsymbol{\vartheta}}\ \ell(\boldsymbol{y} \mid \boldsymbol{\vartheta}))^T\right] \quad (14)$$

where $I(\boldsymbol{\vartheta})$ is the FIM, the expectation is over $\boldsymbol{y}$, and $\ell(\boldsymbol{y} \mid \boldsymbol{\vartheta})$ is the log-likelihood of the observation vector. Through integration by parts, (14) can be rewritten as

$$I(\boldsymbol{\vartheta}) = -\mathbb{E}\left[\nabla_{\boldsymbol{\vartheta}} \nabla_{\boldsymbol{\vartheta}}^T\ \ell(\boldsymbol{y} \mid \boldsymbol{\vartheta})\right]. \quad (15)$$

The CRLB is found by inverting the FIM

$$\mathrm{CRLB}(\boldsymbol{\vartheta}) = I(\boldsymbol{\vartheta})^{-1} \quad (16)$$

where $\boldsymbol{\vartheta}$ are the known or estimated values of the model parameters. Note that the ML estimator is asymptotically unbiased and asymptotically efficient, meaning that as the number of counts goes to infinity, the ML estimate of the parameters reaches the true values ($\hat{\boldsymbol{\vartheta}}_{\mathrm{ML}} \to \boldsymbol{\vartheta}$) and the covariance of the parameter vector reaches the CRLB ($\mathrm{cov}(\hat{\boldsymbol{\vartheta}}_{\mathrm{ML}}) \to I(\boldsymbol{\vartheta})^{-1}$) [30].

The log-likelihood for Poisson distributed observations is

$$\ell(\boldsymbol{y} \mid \boldsymbol{\vartheta}) = \sum_{i=1}^{N_{\mathrm{O}}} \left(y_i \ln\left(\overline{y}_i\right) - \overline{y}_i - \ln(y_i!)\right) \quad (17)$$

where N_{O} is the number of observations. Plugging (17) into (15), we see that

$$I(\boldsymbol{\vartheta}) = \sum_{i=1}^{N_{\mathrm{O}}} \left(\frac{\nabla_{\boldsymbol{\vartheta}}\ \overline{y}_i \nabla_{\boldsymbol{\vartheta}}^T\ \overline{y}_i}{\overline{y}_i}\right) \quad (18)$$

where $\nabla_{\boldsymbol{\vartheta}}\ \overline{y}_i$ is the gradient of $\overline{y}_i$. For the sth source

$$\begin{aligned} \frac{\partial \overline{y}_i}{\partial \alpha_s} &= A_{i,j'(\phi_s)} t_i \\ \frac{\partial \overline{y}_i}{\partial \phi_s} &= \alpha_s t_i \frac{\partial A_{i,j'(\phi_s)}}{\partial \phi_s} \\ \frac{\partial \overline{y}_i}{\partial b_d} &= t_i. \end{aligned} \quad (19)$$

We use a numerical approach to find the derivative of the system response matrix with respect to the sth source position

$$\frac{\partial A_{i,j'(\phi_s)}}{\partial \phi_s} = \frac{A_{i,j'(\phi_s+\Delta\phi)} - A_{i,j'(\phi_s-\Delta\phi)}}{2\Delta\phi}. \quad (20)$$

For the MATADOR system, we find that $\Delta\phi$ can be as large as 1° without any loss of accuracy in calculating $(\partial A_{i,j'(\phi_s)}/\partial \phi_s)$. Plugging in (19) into (18), we find the FIM—the diagonal elements are

$$\begin{aligned} I(\boldsymbol{\vartheta})[\alpha_s, \alpha_s] &= \sum_{i=1}^{N_{\mathrm{O}}} \frac{\left(A_{i,j'(\phi_s)}\right)^2\ t_i}{\sum_{s=1}^{S}\left(\alpha_s A_{i,j'(\phi_s)}\right) + b_i} \\ I(\boldsymbol{\vartheta})[\phi_s, \phi_s] &= \sum_{i=1}^{N_{\mathrm{O}}} \frac{\left(\alpha_s \frac{\partial A_{i,j'(\phi_s)}}{\partial \phi_s}\right)^2\ t_i}{\sum_{s=1}^{S}\left(\alpha_s A_{i,j'(\phi_s)}\right) + b_i}, \quad \text{and} \\ I(\boldsymbol{\vartheta})[b_d, b_d] &= \sum_{i=1}^{N_{\mathrm{O}}} \frac{t_i}{\sum_{s=1}^{S}\left(\alpha_s A_{i,j'(\phi_s)}\right) + b_i}. \end{aligned} \quad (21)$$

APPENDIX B
SYNTHETICALLY CREATING DATA

In a c-TEI system, the response observed by a detector at (12 cm, 0°) to a source at 90° is the same as the response observed by a detector at (12 cm, 90°) to a source at 180° after a +90° rotation of the mask. Thus, to make Fig. 12, we utilized data from detectors at (12 cm, 27°) and (12 cm, 333°) but generated the system response as if the detector was at (12 cm, 0°) and reconstructed the image.

Since we only have data from the detectors shown in Fig. 4, we cannot synthetically create any source scene. If we want to reconstruct an image using data collected from the outer ring of detector positions, then the sources can only be synthetically rotated by integer multiples of 9°.

Note that this method assumes uniform detector performance with respect to incident particle direction. In general, this assumption is not true for stilbene because of its anisotropic response, but since the anisotropy predominately affects the detection efficiency of the crystal [35] and not the shape of the detector response (efficiency as a function of lateral position, see [8]), the localization precision and angular resolution of the system will not change significantly.

APPENDIX C
SUPPLEMENTAL MATERIAL FOR THE MULTIPLE SOURCE EXPERIMENT

In the multiple-source experiment, radioactive objects were constructed using the following sources.

1) Pu-240 plates. Each plate is 0.32 cm × 5.08 cm × 7.62 cm and contains ~23.9 g of Pu-240 [36].
2) MOX fuel pins (MOX pin ID 129). Each fuel pin is 15.24 cm in length by 0.95 cm in diameter. The pins contain ~3.6 g of Pu-240 [37].

There are five objects of interest in the multiple source setup.

1) MOX fuel canister: at (90 cm, 180°), there are 32 MOX fuel pins arranged in a lattice [38]. The fuel pins are inside of a 0.4-cm-thick steel container. The MOX fuel canister is significantly hotter than any other object in the FOV.
2) Pu-240 stack #1: at (150 cm, 160°), there are 5 Pu-240 plates stacked one on top of the other. The 5.08 cm × 7.62 cm planes are in contact and the 0.32 cm edge is

Authorized licensed use limited to: University of Michigan Library. Downloaded on April 18,2021 at 16:44:55 UTC from IEEE Xplore. Restrictions apply.

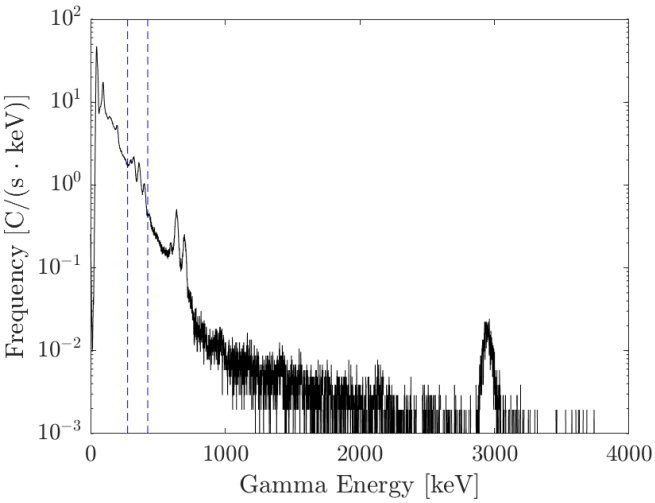

Fig. 22. Gamma-ray energy spectrum collected using the CLLBC detector during the multiple source experiment.

facing MATADOR. This object is shielded by 0.32 cm of tin and 0.64 cm of copper.

3) Pu-240 stack #2: at (150 cm, 200°), there are five Pu-240 plates stacked one on top of the other. The 5.08 cm × 7.62 cm planes are in contact and the 0.32 cm edge is facing MATADOR. This object is shielded by 0.32 cm of tin and 0.64 cm of copper.
4) Line source: centered at (120 cm, 270°), there are four Pu-240 plates placed in a line. The 7.62 cm × 0.32 cm long sides are in contact and the 5.08 cm edge of each plate is facing MATADOR. From the perspective of MATADOR, the source is 9.7° wide. This object is shielded by 0.32 cm of tin and 0.64 cm of copper.
5) Two sources: centered at (80 cm, 90°), there are two stacks of two Pu-240 plates placed 10.2 cm apart. Within each stack, each plate is standing on its 7.62 cm × 0.32 cm edge and the 7.62 cm × 5.08 cm planes are in contact. The stacks are sandwiched between 20.32 cm × 10.16 cm × 5.08 cm lead bricks. From the perspective of MATADOR, the two stacks of Pu-240 plates appear as two point sources separated by 8°. This object is shielded by 1.27 cm of copper.

Fig. 22 shows the energy spectrum of pulses collected when the detector was centered. Note that the pulses near 3 MeV are from thermal neutrons (i.e., $^6\mathrm{Li}(n,\alpha)^3\mathrm{T}$ reaction) not gamma rays. Only pulses within the dashed lines were used for image reconstruction.

Acknowledgment

The authors would like to thank Jay Hix, Dr. Scott Thompson, and the team at Idaho National Laboratory for facilitating the measurements at the Zero Power Physics Reactor facility. This article describes objective technical results and analysis. Any subjective views or opinions that might be expressed in the article do not necessarily represent the views of the U.S. Department of Energy or the United States Government.

References

[1] K. P. Ziock, "Principles and applications of gamma-ray imaging for arms control," *Nucl. Instrum. Meth. Phys. Res. A, Accel. Spectrom. Detect. Assoc. Equip.*, vol. 878, pp. 191–199, Jan. 2018.
[2] R. C. Runkle, "Neutron sensors and their role in nuclear nonproliferation," *Nucl. Instrum. Meth. Phys. Res. A, Accel. Spectrom. Detect. Assoc. Equip.*, vol. 652, no. 1, pp. 37–40, Oct. 2011.
[3] P. Hausladen, M. A. Blackston, E. Brubaker, D. Chichester, P. Marleau, and R. J. Newby, "Fast-neutron coded-aperture imaging of special nuclear material configurations," in *Proc. 53rd Annu. Meeting (INMM)*, 2012, pp. 1–10. [Online]. Available: https://inldigitallibrary.inl.gov/sites/sti/sti/5517228.pdf
[4] M. Blackston, B. L. Brown, E. Brubaker, P. Hausladen, P. Marleau, and R. J. Newby, "Fast-neutron coded-aperture imaging for warhead counting," in *Proc. INMM 52nd Annu. Meeting*, 2011, pp. 1–10.
[5] K. P. Ziock, C. J. Hailey, T. B. Gosnell, J. H. Lupton, and F. A. Harrison, "A gamma-ray imager for arms control," *IEEE Trans. Nucl. Sci.*, vol. 39, no. 4, pp. 1046–1050, Aug. 1992.
[6] X. Liang *et al.*, "Self-supporting design of a time-encoded aperture, gamma-neutron imaging system," *Nucl. Instrum. Meth. Phys. Res. A, Accel. Spectrom. Detect. Assoc. Equip.*, vol. 951, Jan. 2020, Art. no. 162964.
[7] A. Barzilov and A. Guckes, "Time encoded imaging of neutrons and photons using CLYC detector equipped with a dual mode collimator," *Sensors Transducers*, vol. 229, no. 1, pp. 78–83, 2019.
[8] N. P Shah, J. VanderZanden, and D. K. Wehe, "Design and construction of a 1-D, cylindrical, dual-particle, time-encoded imaging system," *Nucl. Instrum. Meth. Phys. Res. A, Accel. Spectrom. Detect. Assoc. Equip.*, vol. 954, Feb. 2020, Art. no. 161785.
[9] J. Brennan *et al.*, "Source detection at 100 meter standoff with a time-encoded imaging system," *Nucl. Instrum. Meth. Phys. Res. A, Accel. Spectrom. Detect. Assoc. Equip.*, vol. 877, pp. 375–383, Jan. 2018.
[10] J. Brennan *et al.*, "Demonstration of two-dimensional time-encoded imaging of fast neutrons," *Nucl. Instrum. Meth. Phys. Res. A, Accel. Spectrom. Detect. Assoc. Equip.*, vol. 802, pp. 76–81, Dec. 2015.
[11] E. E. Fenimore and T. M. Cannon, "Coded aperture imaging with uniformly redundant arrays," *Appl. Opt.*, vol. 17, no. 3, pp. 337–347, 1978.
[12] R. A. Mendez, J. F. Silva, and R. Lobos, "Analysis and interpretation of the Cramér-rao lower-bound in astrometry: One-dimensional case," *Publications Astronomical Soc. Pacific*, vol. 125, no. 927, pp. 580–594, May 2013.
[13] F. Rigaut and B. Neichel, "Multiconjugate adaptive optics for astronomy," *Annu. Rev. Astron. Astrophys.*, vol. 56, no. 1, pp. 277–314, Sep. 2018.
[14] H. W. Babcock, "The possibility of compensating astronomical seeing," *Publications Astronomical Soc. Pacific*, vol. 65, no. 386, pp. 229–236, 1953.
[15] G. J. Gang, J. W. Stayman, T. Ehtiati, and J. H. Siewerdsen, "Task-driven image acquisition and reconstruction in cone-beam CT," *Phys. Med. Biol.*, vol. 60, no. 8, pp. 3129–3150, Apr. 2015.
[16] N. Li and L.-J. Meng, "Adaptive angular sampling for SPECT imaging," *IEEE Trans. Nucl. Sci.*, vol. 58, no. 5, pp. 2205–2218, Oct. 2011.
[17] J. Zhou and J. Qi, "Adaptive imaging for lesion detection using a zoom-in PET system," *IEEE Trans. Med. Imag.*, vol. 30, no. 1, pp. 119–130, Jan. 2011.
[18] H. H. Barrett *et al.*, "Adaptive SPECT," *IEEE Trans. Med. Imag.*, vol. 27, no. 6, pp. 775–788, Jun. 2008.
[19] J. F. Synnevag, A. Austeng, and S. Holm, "Adaptive beamforming applied to medical ultrasound imaging," *IEEE Trans. Ultrason., Ferroelectr., Freq. Control*, vol. 54, no. 8, pp. 1606–1613, Aug. 2007.
[20] L. P. Panych and F. A. Jolesz, "A dynamically adaptive imaging algorithm for wavelet-encoded MRI," *Magn. Reson. Med.*, vol. 32, no. 6, pp. 738–748, Dec. 1994.
[21] A. A. Redwan Newaz, S. Jeong, H. Lee, H. Ryu, and N. Y. Chong, "UAV-based multiple source localization and contour mapping of radiation fields," *Robot. Auto. Syst.*, vol. 85, pp. 12–25, Nov. 2016.
[22] B. Ristic, M. Morelande, and A. Gunatilaka, "Information driven search for point sources of gamma radiation," *Signal Process.*, vol. 90, no. 4, pp. 1225–1239, Apr. 2010.
[23] D. T. Willcox, B. R. Kowash, and D. K. Wehe, "Adaptive imaging using a rotating modulation collimator (RMC)," in *Proc. IEEE Nucl. Sci. Symp. Med. Imag. Conf.*, Oct. 2010, pp. 1531–1535.
[24] J. G. M. FitzGerald, L. W. Burggraf, B. R. Kowash, and E. L. Hull, "A modulating liquid collimator for coded aperture adaptive imaging of gamma-rays," *IEEE Trans. Nucl. Sci.*, vol. 60, no. 3, pp. 2300–2307, Jun. 2013.

Authorized licensed use limited to: University of Michigan Library. Downloaded on April 18,2021 at 16:44:55 UTC from IEEE Xplore. Restrictions apply.

[25] R. Hawrami *et al.*, "$Cs_2LiLa(Br,Cl)_6$ crystals for nuclear security applications," *IEEE Trans. Nucl. Sci.*, vol. 63, no. 2, pp. 509–512, Apr. 2016.

[26] N. Zaitseva *et al.*, "Scintillation properties of solution-grown trans-stilbene single crystals," *Nucl. Instrum. Meth. Phys. Res. A, Accel. Spectrom. Detect. Assoc. Equip.*, vol. 789, pp. 8–15, Jul. 2015.

[27] N. P. Shah, "Adaptive imaging with a cylindrical, time-encoded imaging system," Ph.D. dissertation, Dept. Nucl. Eng. Radiol. Sci., Univ. Michigan, Ann Arbor, MI, USA, 2020.

[28] L. A. Shepp and Y. Vardi, "Maximum likelihood reconstruction for emission tomography," *IEEE Trans. Med. Imag.*, vol. MI-1, no. 2, pp. 113–122, Oct. 1982.

[29] A. J. D. Dekker and A. V. D. Bos, "Resolution: A survey," *J. Opt. Soc. Amer. A, Opt. Image Sci.*, vol. 14, no. 3, pp. 547–557, 1997.

[30] S. M. Kay, *Fundamentals of Statistical Signal Processing: Estimation Theory*. Upper Saddle River, NJ, USA: Prentice-Hall, 1993.

[31] M. Shahram and P. Milanfar, "Statistical and information-theoretic analysis of resolution in imaging," *IEEE Trans. Inf. Theory*, vol. 52, no. 8, pp. 3411–3437, Aug. 2006.

[32] Z. Liu and A. Nehorai, "Statistical angular resolution limit for point sources," *IEEE Trans. Signal Process.*, vol. 55, no. 11, pp. 5521–5527, Nov. 2007.

[33] S. T. Smith, "Statistical resolution limits and the complexified Cramér-Rao bound," *IEEE Trans. Signal Process.*, vol. 53, no. 5, pp. 1597–1609, May 2005.

[34] L. E. Sinclair *et al.*, "End-user experience with the SCoTSS Compton imager and directional survey spectrometer," *Nucl. Instrum. Meth. Phys. Res. A, Accel. Spectrom. Detect. Assoc. Equip.*, vol. 954, Feb. 2020, Art. no. 161683.

[35] P. Schuster, P. Feng, and E. Brubaker, "On the relationship between scintillation anisotropy and crystal structure in pure crystalline organic scintillator materials," *IEEE Trans. Nucl. Sci.*, vol. 65, no. 6, pp. 1292–1306, Jun. 2018.

[36] D. L. Chichester, "Properties of nuclear fuel used in tests with the LLNL gamma-ray mirror in September 2014," Idaho Nat. Lab., Idaho Falls, ID, USA, Tech. Rep. INL/MIS-14-33068, 2014.

[37] D. L. Chichester *et al.*, "Neutron emission characteristics of two mixed-oxide fuels: Simulations and initial experiments," Idaho Nat. Lab., Idaho Falls, ID, USA, Tech. Rep. INL/EXT-09-16566, 2009.

[38] D. L. Chichester, J. Sanders, J. A. Turnage, J. D. West, and M. A. Willmore, "The INL nuclear and radiological activity center," Idaho Nat. Lab., Idaho Falls, ID, USA, Tech. Rep. INL/COM-13-28220, 2013.

Authorized licensed use limited to: University of Michigan Library. Downloaded on April 18,2021 at 16:44:55 UTC from IEEE Xplore. Restrictions apply.